processes

MDPI

Article

Multi-Phase In Silico Discovery of Potential SARS-CoV-2 RNA-Dependent RNA Polymerase Inhibitors among 3009 Clinical and FDA-Approved Related Drugs

Eslam B. Elkaeed [1], Hazem Elkady [2], Amany Belal [3], Bshra A. Alsfouk [4], Tuqa H. Ibrahim [5,6], Mohamed Abdelmoaty [5], Reem K. Arafa [5,6], Ahmed M. Metwaly [7,8,*] and Ibrahim H. Eissa [2,*]

1 Department of Pharmaceutical Sciences, College of Pharmacy, AlMaarefa University, Riyadh 13713, Saudi Arabia; ikaeed@mcst.edu.sa
2 Pharmaceutical Medicinal Chemistry & Drug Design Department, Faculty of Pharmacy (Boys), Al-Azhar University, Cairo 11884, Egypt; hazemelkady@azhar.edu.eg
3 Department of Pharmaceutical Chemistry, College of Pharmacy, Taif University, P.O. Box 11099, Taif 21944, Saudi Arabia; abilalmoh1@yahoo.com
4 Department of Pharmaceutical Sciences, College of Pharmacy, Princess Nourah Bint Abdulrahman University, P.O. Box 84428, Riyadh 11671, Saudi Arabia; baalsfouk@pnu.edu.sa
5 Drug Design and Discovery Laboratory, Zewail City of Science and Technology, Cairo 12578, Egypt; s-tuqa.hamed@zewailcity.edu.eg (T.H.I.); mohamed.moatyy@gmail.com (M.A.); rkhidr@zewailcity.edu.eg (R.K.A.)
6 Biomedical Sciences Program, University of Science and Technology, Zewail City of Science and Technology, Cairo 12578, Egypt
7 Pharmacognosy and Medicinal Plants Department, Faculty of Pharmacy (Boys), Al-Azhar University, Cairo 11884, Egypt
8 Biopharmaceutical Products Research Department, Genetic Engineering and Biotechnology Research Institute, City of Scientific Research and Technological Applications (SRTA-City), Alexandria 21934, Egypt
* Correspondence: ametwaly@azhar.edu.eg (A.M.M.); ibrahimeissa@azhar.edu.eg (I.H.E.)

check for updates

Citation: Elkaeed, E.B.; Elkady, H.; Belal, A.; Alsfouk, B.A.; Ibrahim, T.H.; Abdelmoaty, M.; Arafa, R.K.; Metwaly, A.M.; Eissa, I.H. Multi-Phase In Silico Discovery of Potential SARS-CoV-2 RNA-Dependent RNA Polymerase Inhibitors among 3009 Clinical and FDA-Approved Related Drugs. *Processes* **2022**, *10*, 530. https://doi.org/10.3390/pr10030530

Academic Editors: Antony Kam, Shining Loo and Simon Ming-Yuen Lee

Received: 9 February 2022
Accepted: 1 March 2022
Published: 7 March 2022

Publisher's Note: MDPI stays neutral with regard to jurisdictional claims in published maps and institutional affiliations.

Abstract: Proceeding our prior studies of SARS-CoV-2, the inhibitory potential against SARS-CoV-2 RNA-dependent RNA polymerase (RdRp) has been investigated for a collection of 3009 clinical and FDA-approved drugs. A multi-phase in silico approach has been employed in this study. Initially, a molecular fingerprint experiment of Remdesivir (RTP), the co-crystallized ligand of the examined protein, revealed the most similar 150 compounds. Among them, 30 compounds were selected after a structure similarity experiment. Subsequently, the most similar 30 compounds were docked against SARS-CoV-2 RNA-dependent RNA polymerase (PDB ID: 7BV2). Aloin **359**, Baicalin **456**, Cefadroxil **1273**, Sophoricoside **1459**, Hyperoside **2109**, and Vitexin **2286** exhibited the most precise binding modes, as well as the best binding energies. To confirm the obtained results, MD simulations experiments have been conducted for Hyperoside **2109**, the natural flavonoid glycoside that exhibited the best docking scores, against RdRp (PDB ID: 7BV2) for 100 ns. The achieved results authenticated the correct binding of **2109**, showing low energy and optimum dynamics. Our team presents these outcomes for scientists all over the world to advance in vitro and in vivo examinations against COVID-19 for the promising compounds.

Keywords: SARS-CoV-2 RNA-dependent RNA polymerase; FDA-approved drugs; molecular fingerprints; structural similarity; molecular docking; MD simulations

1. Introduction

The WHO reported on 4 February 2022 that the confirmed global infected cases of SARS-CoV-2 were 386,548,962. Unfortunately, 5,705,754 of that total passed away [1]. To respond to these alarming numbers, extensive work is required from scientists globally to discover a cure.

The FDA approval of any drug means that the drug's effect and side effects have been judged by the Center for Drug Evaluation and Research (CDER) in the FDA [2]. Accordingly, FDA approval indicates the efficacy and the general safety of that drug [3]. Hence, FDA-approved drugs could be an invaluable source in drug discovery, as they can be repurposed to be utilized for alternate functions [4]. Whereas the traditional drug discovery process costs an average of 2.6 billion USD over twelve years [5], computational or in silico screening can be utilized efficiently and effectively to discover new drugs [6,7].

Ligand-based virtual screening is an in silico approach in which the software utilizes the chemical structure of an active molecule as a reference. This reference is utilized and based on the principles of the Structure–Activity Relationship (SAR), which anticipates the activity of other molecules with unidentified or different known activity [8]. Ligand-based in silico methods have been employed across different fields of drug design and discovery, such as in molecular design [9,10], rational drug design [11–16], computational chemistry [17,18], docking [19,20], DFT [21–23] evaluation, toxicity [24–26], and ADME-Tox [27–29]. In addition, molecular dynamic simulation is considered one of the most efficient computational techniques that confirms the affinity of a compound to a particular receptor [30,31].

Our team utilized ligand-based in silico methods to discover potential inhibitors for COVID-19 essential enzymes. We described the potential inhibitions of a big group of isoflavonoids [32] in addition to the natural metabolites that were isolated from *Monanchora* sp. [33] and *Artemisia sublessingiana* [34]. Likewise, we reported a multi-stage in silico method (ligand- and structure-based) to identify the best potential SARS-CoV-2 nsp10 inhibitor of 310 antiviral natural compounds [35]. The same method decided the most potential semisynthetic compound of 69 ligands against SARS-CoV-2 PLpro [36].

In this manuscript, 3009 clinical and FDA-approved drugs have been utilized as an exam group to explore the most potent SARS-CoV-2 RdRp inhibitors, depending on a multi-stage in silico method (ligand- and structure-based). All the tested drugs were obtained from approved institutions such as the FDA (U.S. Food and Drug Administration, Sliver Spring, MD, USA), EMA (European Medicines Agency, Amsterdam, The Netherlands, European), HMA (Heads of Medicines Agency, Amsterdam, The Netherlands, European), CFDA (China Food and Drug Administration, Beijing, China), PMDA (Pharmaceuticals and Medical Devices Agency, Tokyo, Japan), pharmacopeias such as USP, BP, EP, JP, and Ph, or from Selleckchem.com (https://www.selleckchem.com/screening/fda-approved-drug-library.html, accessed on 1 October 2021) The employed method started with the similarity detection of the test group with the co-crystallized ligand (RTP) of SARS-CoV-2 RdRp, utilizing molecular fingerprint and structure similarity studies. Then, the binding modes of the selected compounds were examined by molecular docking and confirmed by molecular dynamic (MD) simulation experiments.

2. Results and Discussion

2.1. Molecular Fingerprint Study

Molecular fingerprinting is a type of ligand-based in silico study that links the biological activities of the tested molecules to their chemical structures [37]. It is based on the scientific basics of the Structure–Activity Relationship (SAR). Agreeing with the principle of SAR, the likeness in the chemical structure of two molecules is predicted to be linked to a likeness in bioactivity [38]. We herein considered the co-crystallized ligand, RTP, as a reference due to its high binding affinity with SARS-CoV-2 RdRp (PDB ID: 7BV2). Consequently, molecules that have similar chemical structures to RTP are predicted to exhibit a high binding affinity that inhibits the target protein.

In the fingerprint study, the software extracts chemical and physical descriptors of the examined and reference molecules, and the presence and/or the absence of these descriptors is calculated for all atoms. The calculation of the tested descriptors is performed by converting it to bit strings (mathematical symbols). The obtained strings are used to compare and expect the likeness [39,40]. Discovery Studio software has been employed to

reveal the similarity of the fingerprints of RTP with 3009 FDA-approved drugs. The experiment was adapted to select the highest 5% (150) of compounds in similarity (Table 1). The following descriptors were investigated in the atoms as well as fragments of the examined molecules and **RTP**: H-bond acceptors [41], H-bond donors [42], charges [43], hybridization [44], positive ionizable atoms [45], negative ionizable atoms [46], halogens [47], and aromatic groups [48] aligned with the ALogP [49].

Table 1. Fingerprint similarity between the FDA-approved compounds and RTP.

Comp.	Similarity	SA	SB	SC	Comp.	Similarity	SA	SB	SC
RTP	1	206	0	0	**2140**	0.513672	263	306	−57
4	0.532394	189	149	17	**1880**	0.493976	205	209	1
42	0.522523	116	16	90	**736**	0.492163	157	113	49
50	0.589	136	25	70	**2232**	0.508159	218	223	−12
56	0.682	161	30	45	**1345**	0.51358	208	199	−2
152	0.55	121	14	85	**2483**	0.498371	153	101	53
159	0.516129	160	104	46	**2474**	0.4875	117	34	89
186	0.571	128	18	78	**1268**	0.503937	192	175	14
199	0.515306	202	186	4					
241	0.586	130	16	76	**537**	0.507692	198	184	8
310	0.586	130	16	76	**549**	0.507519	135	60	71
365	0.606	154	48	52	**51**	0.513274	116	20	90
374	0.529617	152	81	54	**2399**	0.49359	154	106	52
410	0.601	155	52	51	**2186**	0.513253	213	209	−7
435	0.52	143	69	63	**2496**	0.489971	171	143	35
446	0.585	162	71	44	**1075**	0.50646	196	181	10
447	0.54013	249	255	−43	**380**	0.496575	145	86	61
450	0.577	138	33	68	**1802**	0.504785	211	212	−5
458	0.557252	146	56	60	**1807**	0.5	196	186	10
461	0.541096	158	86	48	**807**	0.496711	151	98	55
502	0.606	154	48	52	**1747**	0.513274	174	133	32
539	0.559809	117	3	89	**1411**	0.501458	172	137	34
573	0.520661	189	157	17	**1332**	0.490476	206	214	0
621	0.518182	114	14	92	**2573**	0.488189	186	175	20
659	0.562963	152	64	54	**470**	0.501458	172	137	34
711	0.568	126	16	80	**2286**	0.5025	201	194	5
723	0.59	135	23	71	**2009**	0.508197	124	38	82
777	0.519313	121	27	85	**1405**	0.488889	132	64	74
788	0.521531	218	212	−12	**937**	0.490617	183	167	23
856	0.52231	199	175	7	**951**	0.491525	145	89	61
874	0.535377	227	218	−21	**2111**	0.495516	221	240	−15
928	0.6	204	134	2	**359**	0.511002	209	203	−3
1017	0.543554	156	81	50	**1789**	0.497696	216	228	−10
1163	0.523546	189	155	17	**2988**	0.492447	163	125	43
1232	0.533762	166	105	40	**625**	0.494949	196	190	10

Table 1. *Cont.*

Comp.	Similarity	SA	SB	SC	Comp.	Similarity	SA	SB	SC
1273	0.541139	171	110	35	**1226**	0.497238	180	156	26
1369	0.603	149	41	57	**919**	0.513274	116	20	90
1391	0.566	214	172	−8	**1911**	0.501672	150	93	56
1445	0.542169	135	43	71	**734**	0.497653	212	220	−6
1458	0.526144	161	100	45	**1702**	0.493548	153	104	53
1459	0.516291	206	193	0	**2999**	0.487524	254	315	−48
1478	0.535503	181	132	25	**2751**	0.495751	175	147	31
1496	0.53211	116	12	90	**371**	0.493639	194	187	12
1569	0.519722	224	225	−18	**2023**	0.488971	133	66	73
1595	0.577	120	2	86	**2921**	0.504043	187	165	19
1631	0.568	147	53	59	**2886**	0.502825	178	148	28
1651	0.566	291	308	−85	**618**	0.501832	137	67	69
1728	0.516605	140	65	66	**456**	0.487864	201	206	5
1732	0.554264	143	52	63	**1068**	0.498812	210	215	−4
1778	0.555556	180	118	26	**1723**	0.498812	210	215	−4
1812	0.518395	155	93	51	**189**	0.488889	110	19	96
1858	0.5179	217	213	−11	**1490**	0.488189	186	175	20
1917	0.598	171	80	35	**1839**	0.509537	187	161	19
1918	0.577	138	33	68	**1662**	0.504098	123	38	83
2017	0.678	183	64	23	**997**	0.51358	208	199	−2
2031	0.545455	132	36	74	**638**	0.498084	130	55	76
2042	0.6	150	44	56	**1669**	0.51046	122	33	84
2056	0.553191	130	29	76	**786**	0.498623	181	157	25
2176	0.601	176	87	30	**2024**	0.512121	169	124	37
2233	0.675	185	68	21	**1610**	0.513441	191	166	15
2268	0.55157	123	17	83	**1584**	0.498567	174	143	32
2376	0.575	138	34	68	**1642**	0.503979	190	171	16
2463	0.520776	188	155	18	**2109**	0.490476	206	214	0
2488	0.55625	178	114	28	**2764**	0.499006	251	297	−45
2501	0.519713	145	73	61	**2850**	0.488889	264	334	−58
2523	0.524476	150	80	56	**883**	0.492823	206	212	0
2585	0.548673	124	20	82	**2420**	0.498099	131	57	75
2612	0.566	159	75	47	**781**	0.501475	170	133	36
2618	0.525773	153	85	53	**679**	0.492908	139	76	67
2732	0.532468	123	25	83	**404**	0.494186	170	138	36
2786	0.556522	128	24	78	**1873**	0.5	157	108	49
2831	0.588	141	34	65	**1185**	0.508143	312	408	−106
2844	0.542986	120	15	86	**2980**	0.497674	107	9	99
2876	0.631	210	127	−4	**2104**	0.513308	135	57	71
2879	0.577	138	33	68	**663**	0.505291	191	172	15
2991	0.581	312	331	−106	**498**	0.506143	206	201	0

SA: The number of shared bits in both RTP and the examined molecule. **SB**: The number of present bits in the examined molecule but not RTP. **SC**: The number of present bits in RTP but not the examined molecule.

2.2. Molecular Similarity

Molecular similarity is also another kind of ligand-based in silico study. The molecular similarity study examines the whole chemical structure of both the reference molecule and the experiment set. The study computes different descriptors, which may be topological, electronic, steric, and/or physical [50]. In contrast, the fingerprint study computes the descriptors in atoms or substructures [51]. The selected 150 FDA-approved drugs, after the molecular fingerprint experiment, were subjected to the molecular similarity study of **RTP**, using Discovery studio software. The tested descriptors (Figure 1 and Table 2) were partition coefficient (ALog p) [52], molecular weight (M. W) [53], H-bond donors (HBA) [54], H-bond acceptors (HBD) [55], rotatable bonds number (RB) [56], number of rings (R) and aromatic rings (AR) [57], minimum distance (MD) [58], and the molecular fractional polar surface area (MFPSA) [59]. The study revealed the most similar 1% compounds (**30**) (Figure 2).

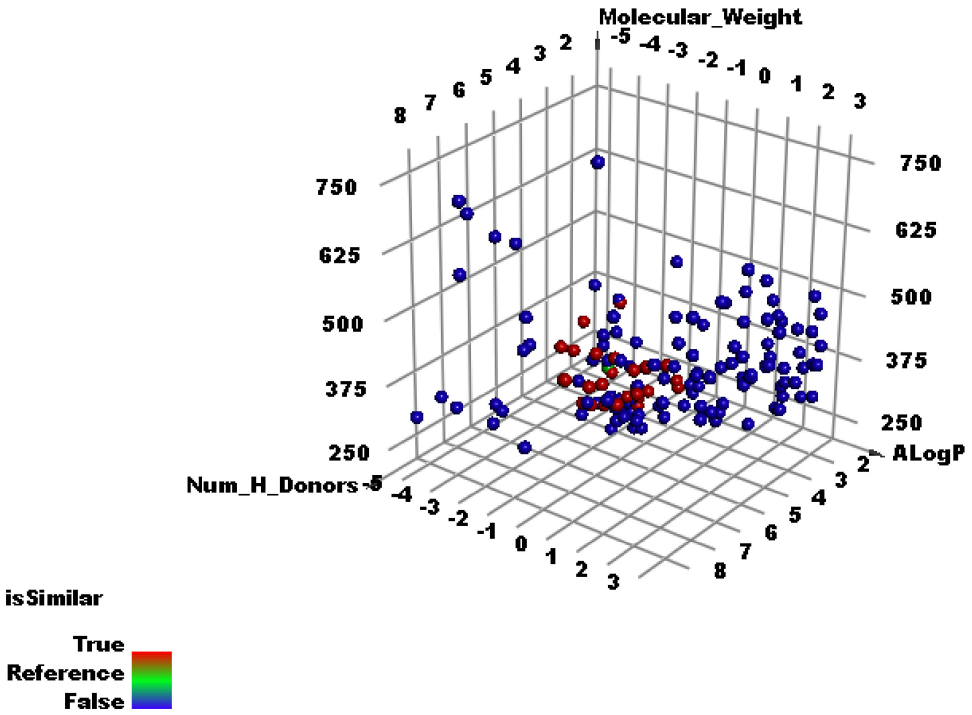

Figure 1. Structural similarity of the FDA-approved compounds and **RTP**.

Table 2. Similarity descriptors of the FDA-approved compounds and **RTP**.

Comp.	ALog p	M. W	HBA	HBD	RB	R	AR	MFPSA	M D
RTP	−1.5	371.24	11	5	4	3	2	0.612	0
50	−1.38	297.27	9	4	3	3	2	0.508	0.516
56	−1.38	365.21	11	5	4	3	2	0.602	0.04
152	−0.77	287.21	8	3	5	2	2	0.502	0.769
186	−1.31	285.23	8	4	2	3	2	0.52	0.638
241	−1.88	267.24	8	4	2	3	2	0.539	0.656
310	−1.88	267.24	8	4	2	3	2	0.539	0.656
359	−0.4	418.39	9	7	3	4	2	0.438	0.775
446	−0.51	340.28	9	5	3	3	1	0.476	0.702
456	0.61	446.36	11	6	4	4	2	0.463	0.695
458	−0.85	328.27	9	5	2	3	1	0.489	0.719
461	−0.34	354.31	9	6	5	2	1	0.487	0.775

Table 2. *Cont.*

Comp.	ALog p	M. W	HBA	HBD	RB	R	AR	MFPSA	M D
498	0.21	432.38	10	6	4	4	2	0.424	0.724
659	−1.61	295.29	8	5	2	3	1	0.521	0.765
723	−2.38	283.24	8	5	2	3	1	0.587	0.76
997	0.45	416.38	9	5	4	4	2	0.384	0.811
1017	−0.43	442.22	11	6	5	3	2	0.459	0.565
1273	−2.7	381.4	8	5	4	3	1	0.501	0.718
1332	−0.3	464.38	12	8	4	4	2	0.499	0.83
1459	0.21	432.38	10	6	4	4	2	0.424	0.724
1917	−3.25	398.44	10	4	7	3	2	0.481	0.657
2017	−2.16	365.24	12	6	4	3	2	0.655	0.284
2042	−2.09	285.26	9	5	2	3	2	0.589	0.491
2109	−0.3	464.38	12	8	4	4	2	0.499	0.83
2176	−1.93	390.35	10	5	4	4	3	0.491	0.675
2233	−2.24	427.2	14	6	6	3	2	0.678	0.582
2286	0.02	432.38	10	7	3	4	2	0.455	0.75
2376	−1.32	269.26	8	4	2	3	2	0.54	0.649
2612	−1.98	460.77	10	4	8	2	2	0.572	0.735
2732	−0.82	299.22	8	3	5	3	2	0.504	0.69
2831	−0.98	305.23	9	4	5	2	2	0.55	0.545

2.3. Docking Studies

The thirty most similar FDA-approved drugs to Remdesivir, the co-crystallized ligand of SARS-CoV-2 RdRp, were docked against the target protein. The carried-out study aims to examine the ability of the selected compounds to bind to and inhibit SARS-CoV-2 RdRp (PDB ID: **7BV2**). The study also investigated the binding free energies as well as the binding modes of the examined FDA-approved drugs. Table 3 illustrates the calculated ΔG (binding free energies) of the tested compounds and the reference drug (Remdesivir) against SARS-CoV-2 RdRp.

Table 3. ΔG values of the FDA-approved drugs and **RTP**.

Comp.	ΔG (kcal/mol)	Comp.	ΔG (kcal/mol)
Remdesivir	−18.65	Brimonidine Tartrate (**1017**)	−15.95
Nelarabine (**50**)	−18.36	Cefadroxil (**1273**)	−21.24
Fludarabine Phosphate (**56**)	−17.73	Isoquercitrin (**1332**)	−23.40
Ramelteon (**152**)	−17.74	Sophoricoside (**1459**)	−21.43
Fludarabine (**186**)	−15.99	Ademetionine (**1917**)	−22.70
Adenosine (**241**)	−16.36	Adenosine 5′-monophosphate monohydrate (**2017**)	−17.73
vidarabine (**310**)	−16.63	Vidarabine monohydrate (**2042**)	−16.63
Aloin (**359**)	−23.11	Hyperoside (**2109**)	−24.46
Esculin (**446**)	−19.26	Regadenoson (**2176**)	−22.85
Baicalin (**456**)	−20.62	ADP (**2233**)	−17.42
Bergenin (**458**)	−19.18	Vitexin (**2286**)	−25.00
Chlorogenic Acid (**461**)	−19.38	2′-Deoxyadenosine monohydrate (**2376**)	−16.33
Puerarin (**498**)	−22.35	Thiamine-pyrophosphate-hydrochloride (**2612**)	−17.78

Table 3. *Cont.*

Comp.	ΔG (kcal/mol)	Comp.	ΔG (kcal/mol)
Entecavir hydrate (**659**)	−18.30	Besifovir (**2732**)	−17.50
Guanosine (**723**)	−16.14	Tenofovir hydrate (**2831**)	−17.26
Daidzin (**997**)	−21.34		

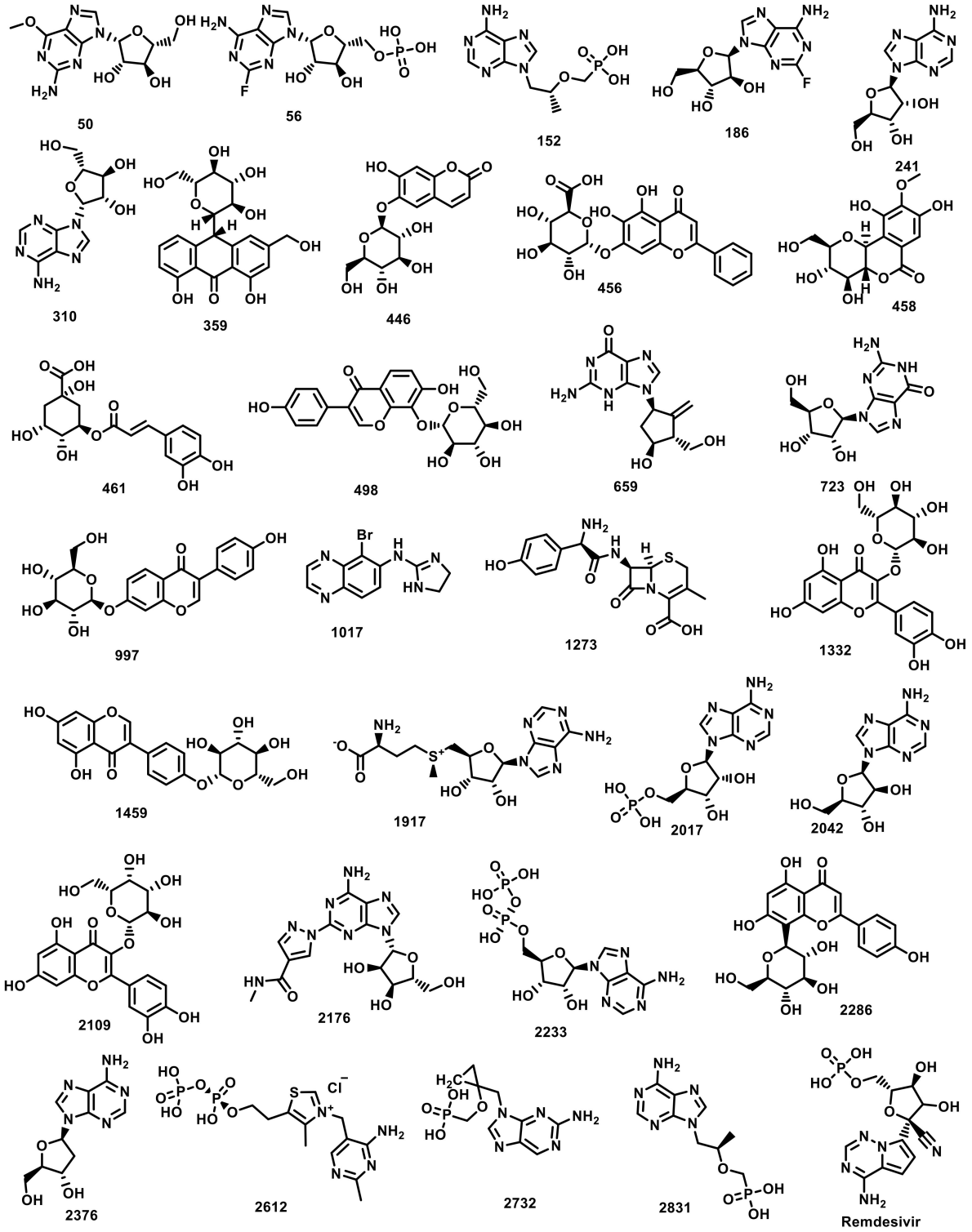

Figure 2. The most similar thirty compounds to RTP.

The docking approach was validated by re-docking Remdesivir against the RdRp-active site. The validation step established the protocol's applicability, as demonstrated by the small RMSD (1.29 Å) between the re-docked pose and the co-crystallized one (Figure 3).

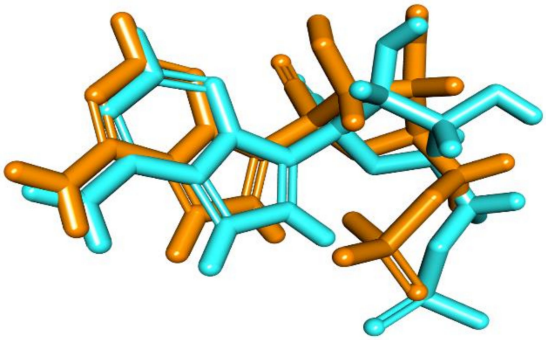

Figure 3. Superimposition of the co-crystallized pose (orange) and the re-docking pose (turquoise) of RTP in the active site of the RdRp.

At first, to understand the docking modes, we have to understand the structure of the SARS-CoV-2 RdRp enzyme. RdRp consists of three main parts. Firstly, an ATP-binding site that is represented by a network of different amino acids, including the key amino acid residue (Arg555). Secondly, an RNA primer that is represented by many nucleotides including uridine 20 (U20), uridine 10 (U10), and adenine 11 (A11). Finally, a pyrophosphate group (POP1003).

The mode of binding of RTP inside the SARS-CoV-2 RdRp is illustrated in Figure 4. It was noticed that RTP interacted with the active site via the formation of four hydrogen bonds (H-bonds), four hydrophobic interactions, and five electrostatic interactions. In detail, the pyrrolo[2,1-*f*][1,2,4]triazin-4-amine moiety interacted with RNA primer, forming four hydrophobic interactions with A11 and U20 and one H-bond with U10. Moreover, the 5-cyano-3,4-dihydroxytetrahydrofuran-2-yl)methyl moiety formed one H- bond with U20. Finally, the dihydrogen phosphate moiety occupied the ATP-binding site, forming one H-bond and one electrostatic interaction with Arg555. Additionally, it formed one H-bond with U20 and two electrostatic interactions with the pyrophosphate group.

The proposed binding mode of **359** revealed an affinity value of −23.11 kcal/mol. The 3,4,5-trihydroxy-6-(hydroxymethyl)tetrahydro-2*H*-pyran moiety was buried in the ATP binding site to form one H-bonds with the key amino acid Arg555. It also interacted with the RNA primer via the formation of two H-bonds with U10. On the other hand, 1,8-dihydroxyanthracen-9(10*H*)-one interacted with the pyrophosphate group via a couple of H-bonds. Moreover, it formed one electrostatic interaction with Arg555 and one pi–pi interaction with U20 (Figure 5).

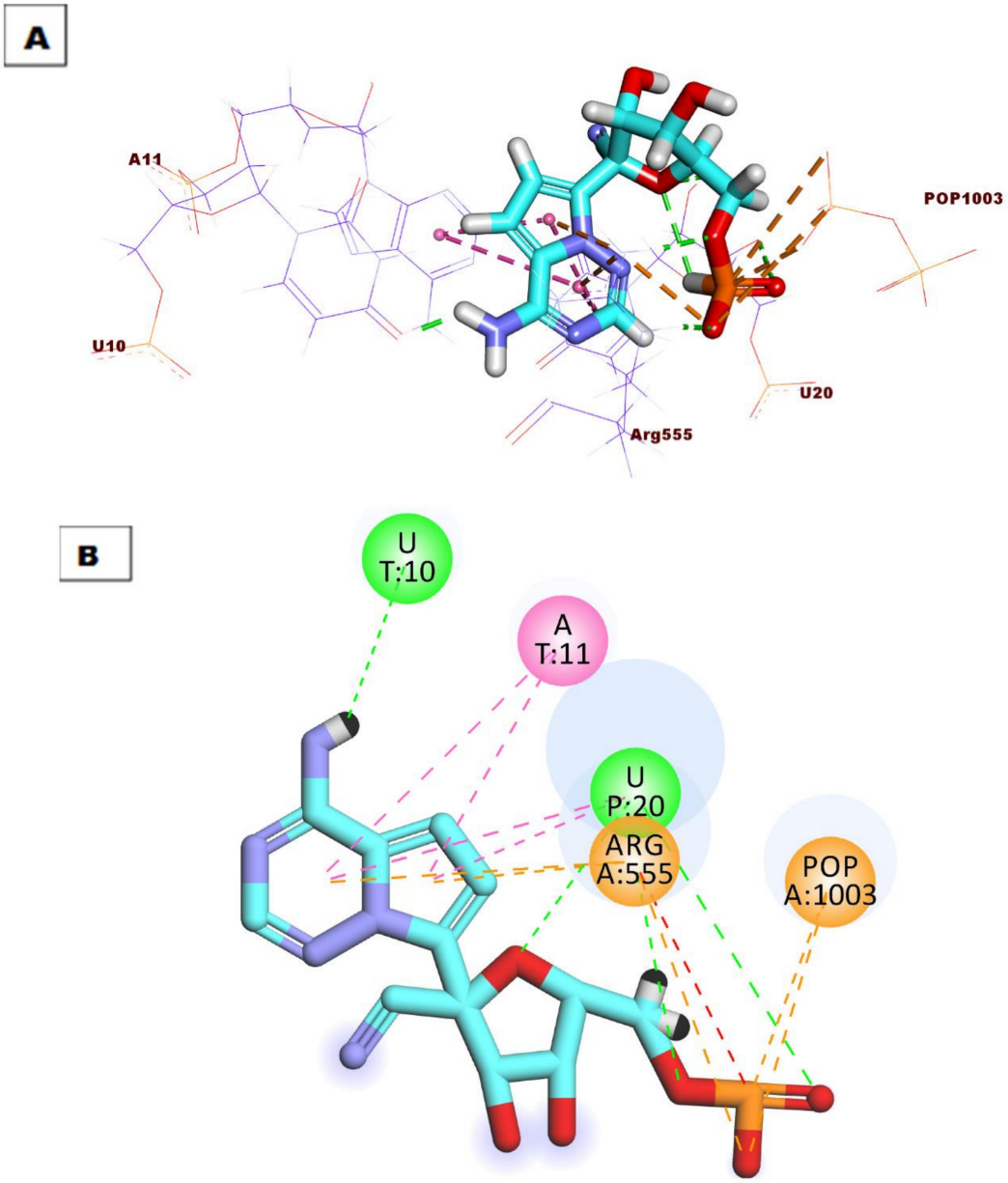

Figure 4. (**A**) 3D binding mode of Remdesivir in the active site of RNA-dependent RNA polymerase. (**B**) 2D binding mode of Remdesivir in the active site of RNA-dependent RNA polymerase.

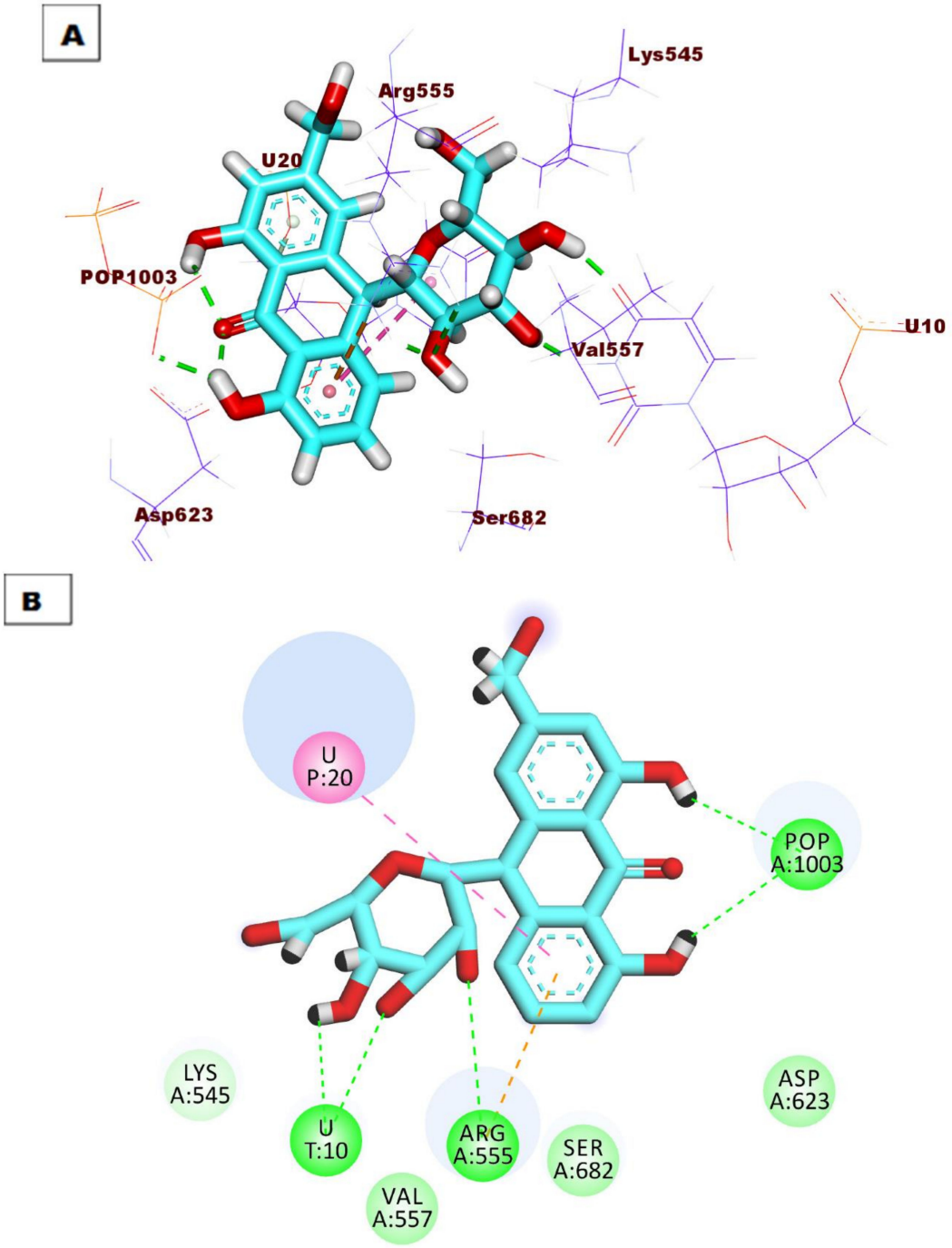

Figure 5. (**A**) 3D binding mode of compound **359** into 7BV2 active site. (**B**) 2D binding mode of compound **359** in the 7BV2 active site.

Compound **456** exerted a binding affinity of −20.52 kcal/mol. It was noticed that 3,4,5-trihydroxytetrahydro-2*H*-pyran-2-carboxylic acid moiety formed two H-bonds with the key amino acid residues in the ATP binding site (Arg555 and Asp760). Additionally, it formed one H-bond with U20 in the RNA primer and another H-bond with pyrophosphate group. Moreover, the 5,6-dihydroxy-4-oxo-2-phenyl-4*H*-chromen moiety was incorporated in the RNA primer, forming two H-bonds and two hydrophobic interactions with U10 and A11, respectively. Additionally, it formed two electrostatic interactions with Arg555 in the ATP-binding site (Figure 6).

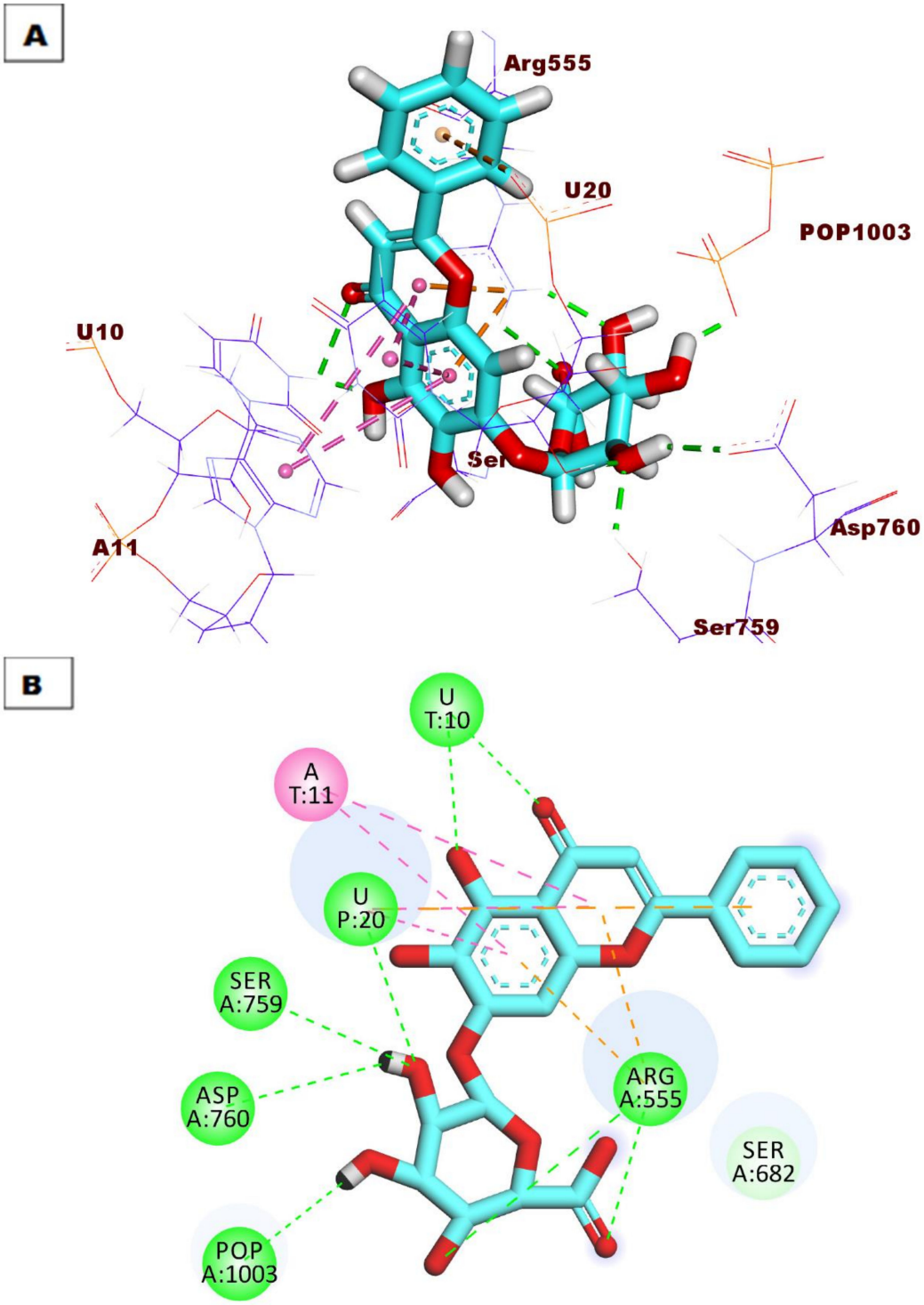

Figure 6. (**A**) 3D binding mode of compound **456** into 7BV2 active site. (**B**) 2D binding mode of compound **456** in the 7BV2 active site.

The docking simulation of compound **2109** revealed that it fit well into the enzyme active site, with a docking score of −24.46 kcal/mol. The ATP-binding site was occupied by the 3-(3,4,5-trihydroxy-6-(hydroxymethyl)tetrahydro-2*H*-pyran-2-yl)oxy) moiety through the formation of four H-bonds with Arg555, Asp760, Asp691, and Ser759. Moreover, the RNA primer was occupied with 2-(3,4-dihydroxyphenyl)4*H*-chromen-4-one moiety via formation of one H-bond, one electrostatic, and one hydrophobic interaction with U10 and U20, respectively. Likewise, the later moiety formed one H-bond with the pyrophosphate

group via its 7-hydroxy group. Such a binding pattern encourages us to study the MD simulation of this member over the rest of the candidates (Figure 7).

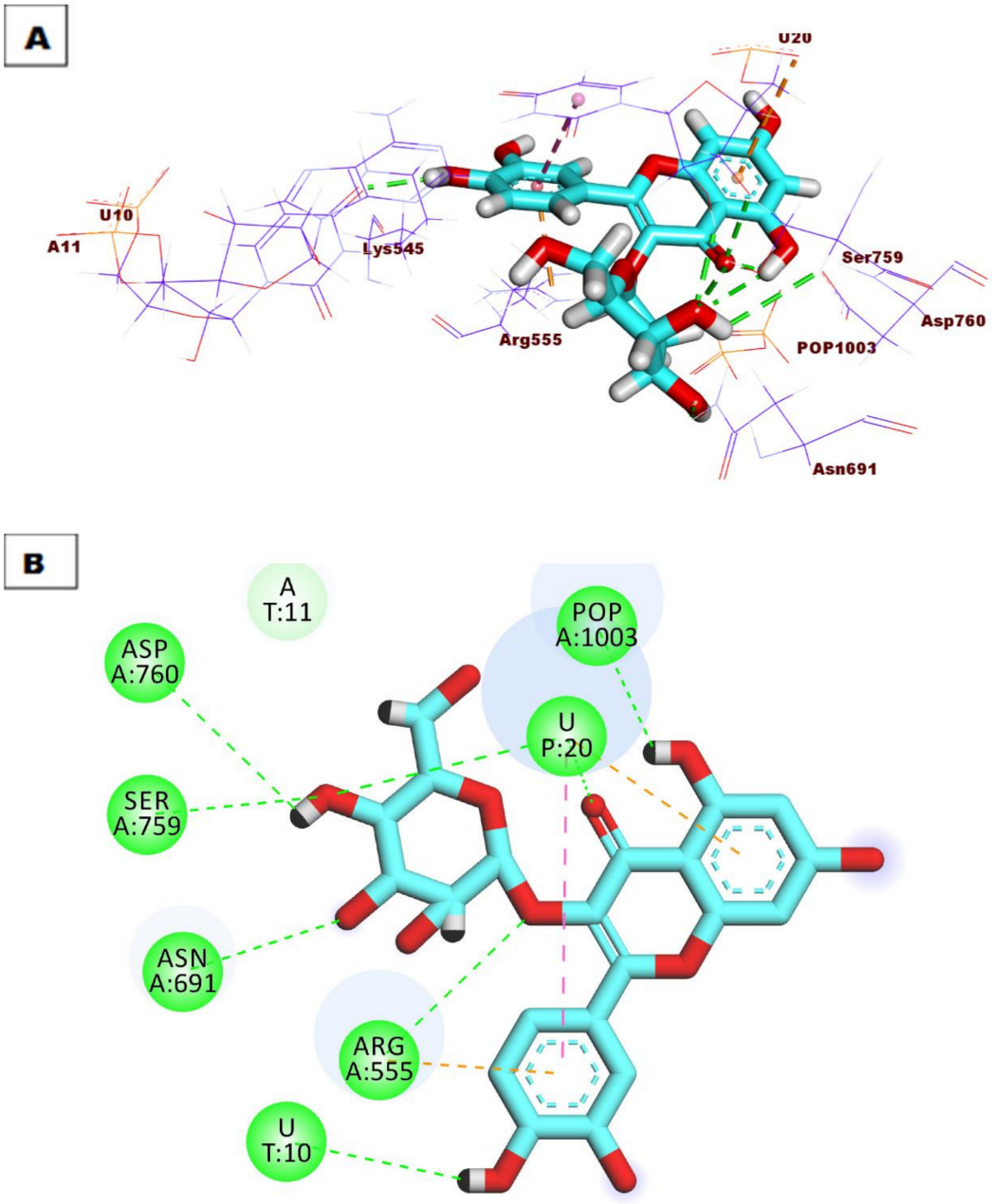

Figure 7. (**A**) 3D binding mode of compound **2109** into 7BV2 active site. (**B**) 2D binding mode of compound **2109** in the 7BV2 active site.

Compound **2286** displayed the highest binding energy score among the series with $\Delta G = -25.00$ kcal/mol. This high binding affinity is presumably attributed to the formation of many hydrophobic, electrostatic, and H-bonding interactions. The chromen-4-one moiety interacted with the RNA primer via the formation of four pi–pi interactions with the key nucleotide U20 and A11. Moreover, it reacted with Arg555 and Ser682, forming two electrostatic interactions and one H-bond, respectively. The sugar moiety (2*H*-pyran) formed two extra H-bonds with Asn691 and the pyrophosphate group (Figure 8).

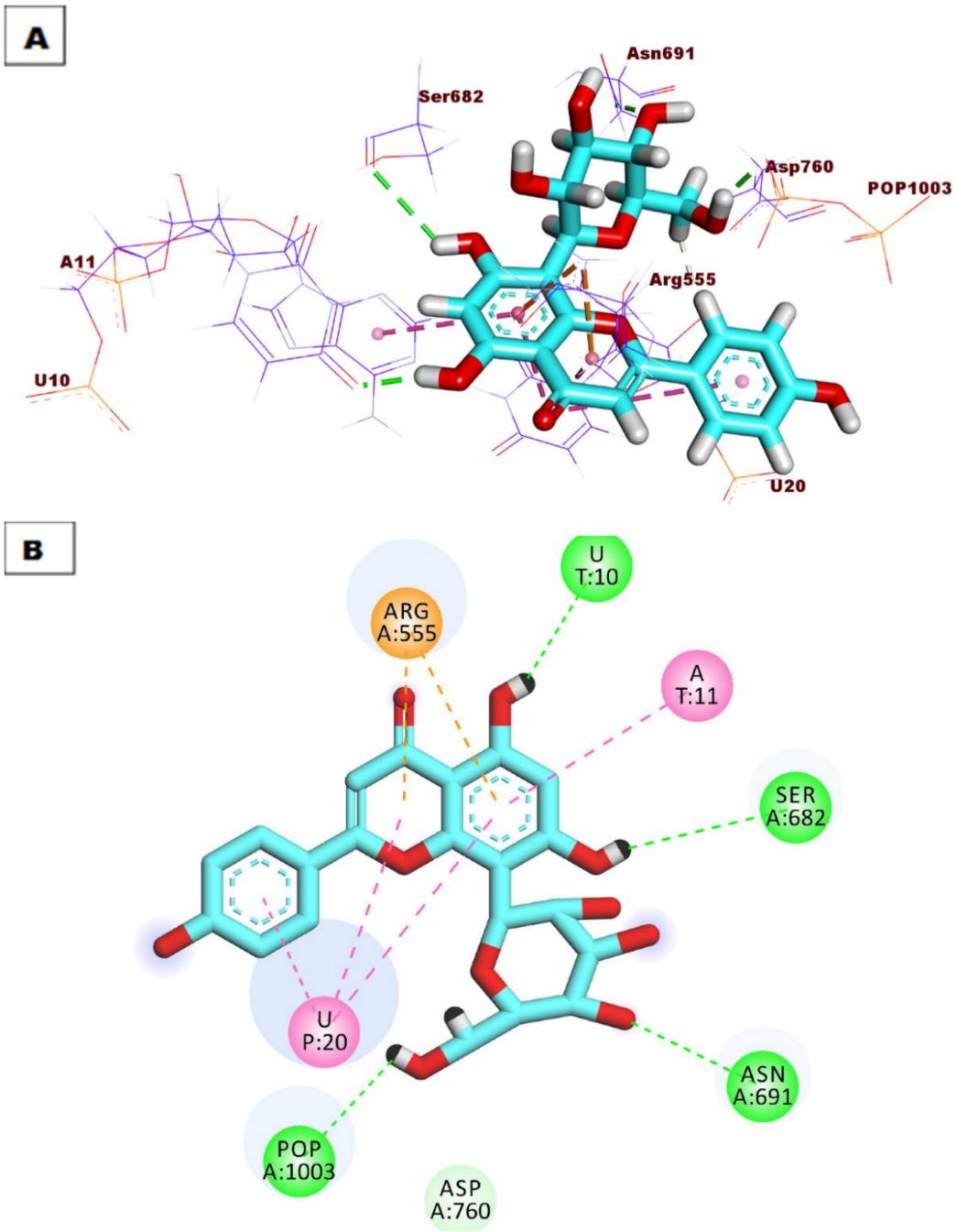

Figure 8. (**A**) 3D binding mode of compound **2286** into 7BV2 active site. (**B**) 2D binding mode of compound **2286** in the 7BV2 active site.

The docking poses accomplished by compound **1273** (ΔG = −21.24 kcal/mol) produced key interactions in the RdRp active sites via the formation of seven H-bonds with U20, U10, Arg555, Asn691, and the Pyrophosphate group. Additionally, it formed one electrostatic with Arg555 and one pi–pi interaction with U20 (Figure 9).

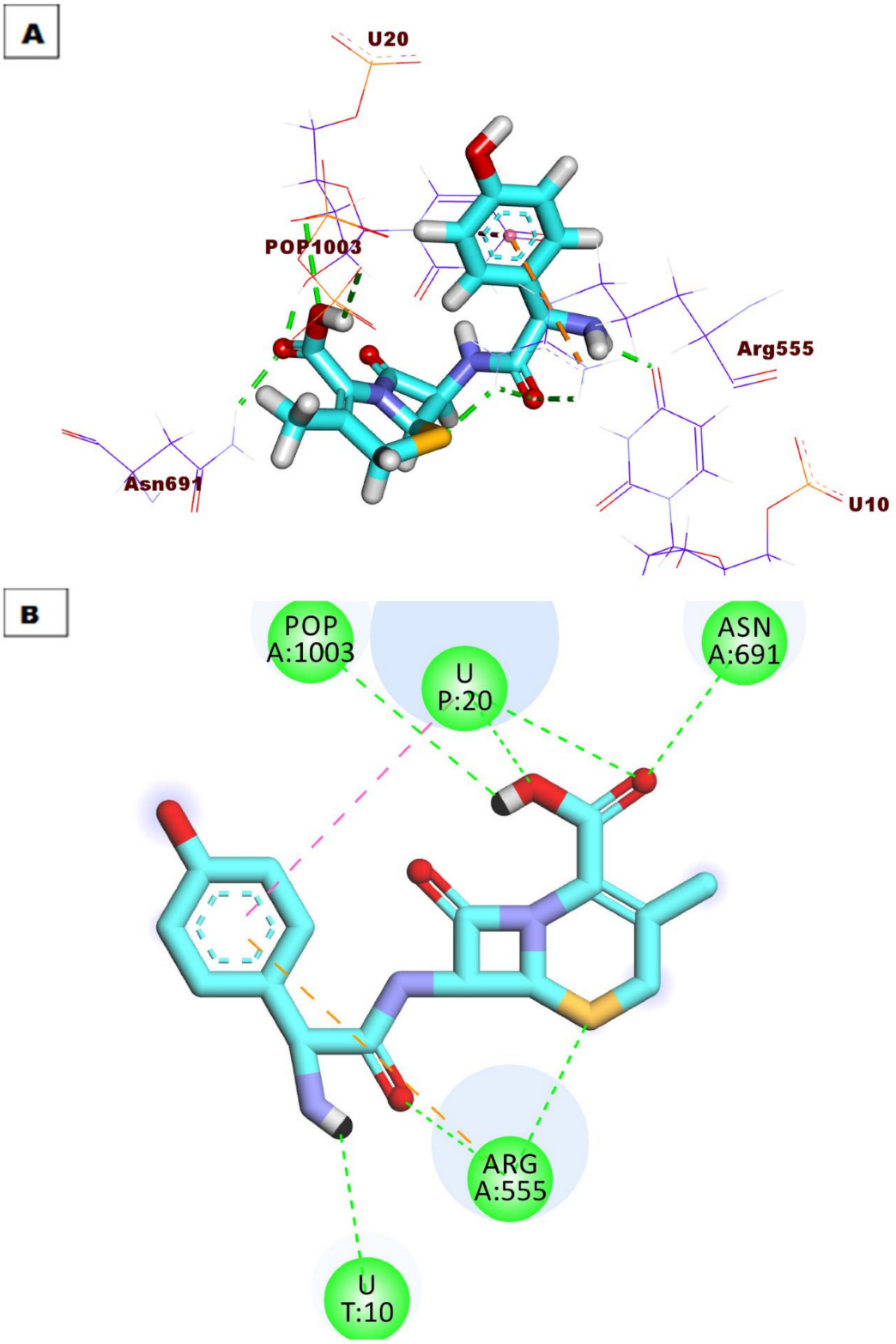

Figure 9. (**A**) 3D binding mode of compound **1273** into 7BV2 active site. (**B**) 2D binding mode of compound **1273** in the 7BV2 active site.

As illustrated in Figure 10, compound **1459** (ΔG = −21.43 kcal/mol) possessed a significant potential binding affinity to the RdRp. It was buried in the ATP-binding site to form three H-bonds with Arg555, Thr680, and Cys622 and one pi–pi interaction with Cys622.

Moreover, compound **1459** interacted with the RNA primer to form three H-bonds with U10 and U20. Finally, it formed one electrostatic interaction with the pyrophosphate group.

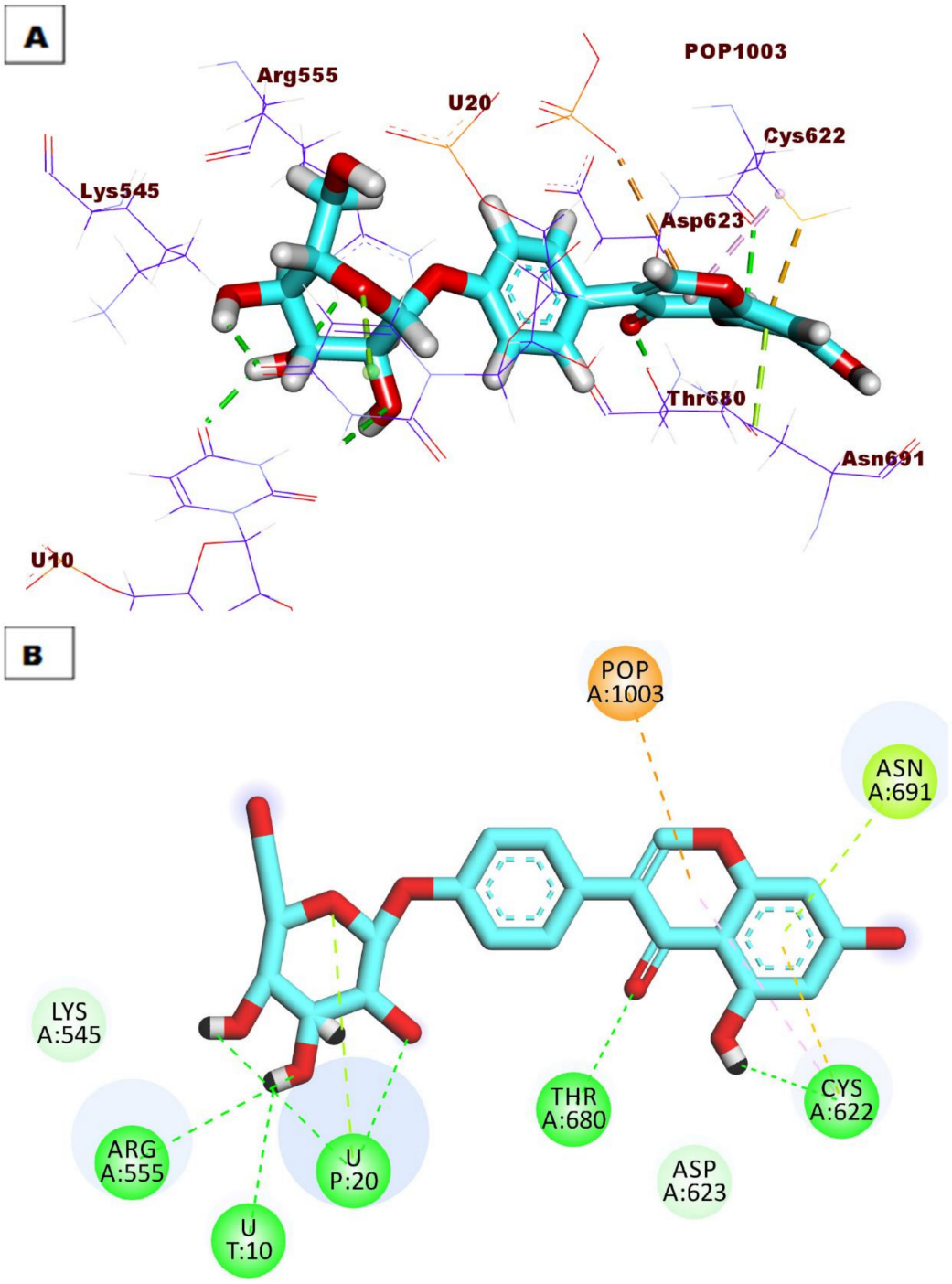

Figure 10. (**A**) 3D binding mode of compound **1459** into 7BV2 active site. (**B**) 2D binding mode of compound **1459** in the 7BV2 active site.

2.4. Molecular Dynamic Simulations

Compound **2109**, Hyperoside, is a natural flavonoid of galactoside (Quercetin 3-galactoside) (Figure 11). Interestingly, the inhibitory effect of hyperoside against COVID-19 has recently been reported as a key molecule in the Chinese Qing-Fei-Pai-Du herbal formula [60]. Additionally, hyperoside inhibited HBV in vivo and in vitro through the inhibition of inhibitors of HBsAg and HBeAg, and decreased DHBV-DNA levels [61]. Ad-

ditionally, hyperoside showed anti-inflammatory activities via the inhibition of the NF-κB signaling pathway [62].

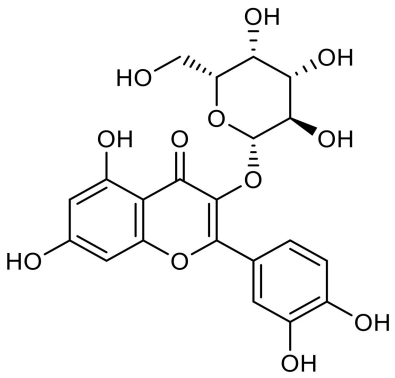

Figure 11. Chemical structure of hyperoside.

The trajectory obtained from the 100 ns MD simulation was analyzed using GROMACS and VMD to check the integrity of the system and examine the stability and strength of hyperoside-SARS-CoV-2 RdRp binding throughout the simulation. Firstly, the radius of gyration of SARS-CoV-2 RdRp was estimated to range from 2.85 to 2.92 nm (Figure 12). The obtained values indicate that SARS-CoV-2 RdRp remained compact and stably folded throughout the simulation.

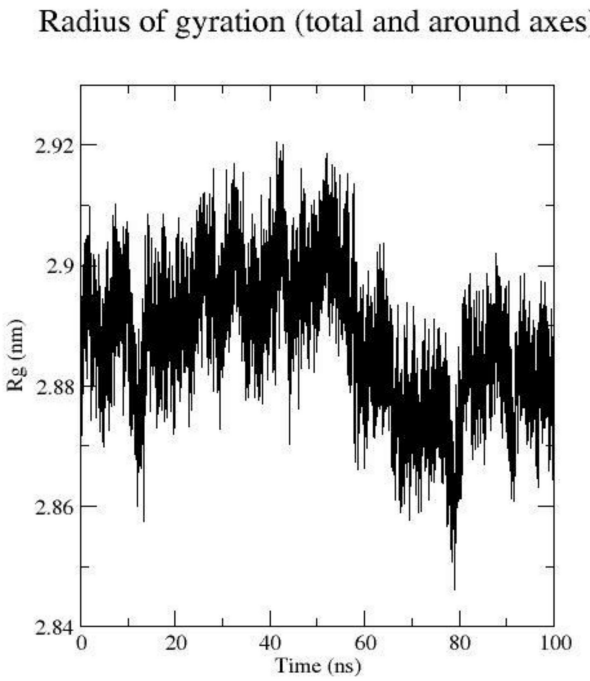

Figure 12. Radius of gyration of SARS-CoV-2 RdRp when complexed with hyperoside, calculated over the course of a 100 ns MD simulation.

The RMSD profile of SARS-CoV-2 RdRp was found to be nearly invariable (Figure 13), implying that its structure is relatively stable during the simulation. The RMSD profile of hyperoside (Figure 14) implies only minor conformational and positional changes relative to the protein backbone. These results were confirmed by visualizing the trajectory using VMD.

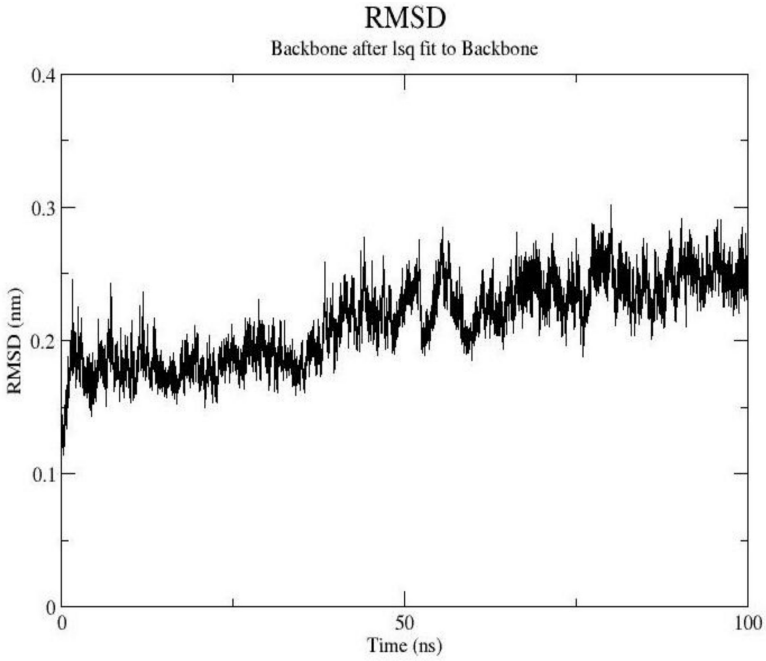

Figure 13. The RMSD of SARS-CoV-2 RdRp with reference to its backbone, calculated over the course of the 100 ns simulation.

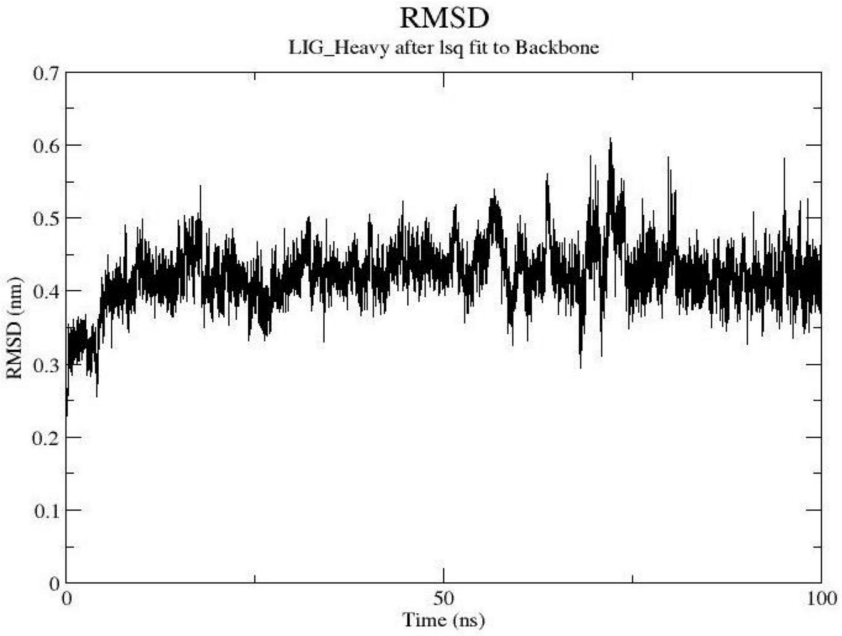

Figure 14. The RMSD of hyperoside with reference to SARS-CoV-2 RdRp backbone, calculated over the course of the 100 ns simulation.

Additionally, the SARS-CoV-2 RdRp-hyperoside interaction was analyzed to measure its strength as an indication of the ligand's affinity towards the protein.

The Coulomb interaction (Coulomb force or electrostatic force) is a physical parameter that describes the magnitude of the electrostatic interaction force between two charged points. The Coulomb interaction is directly proportional to the electrical charge magnitudes and inversely proportional to the distance between them [63]. The energetics analysis showed that the average Coulombic interaction energy between hyperoside and SARS-CoV-2 RdRp was −131.994 kJ/mol (Figure 15).

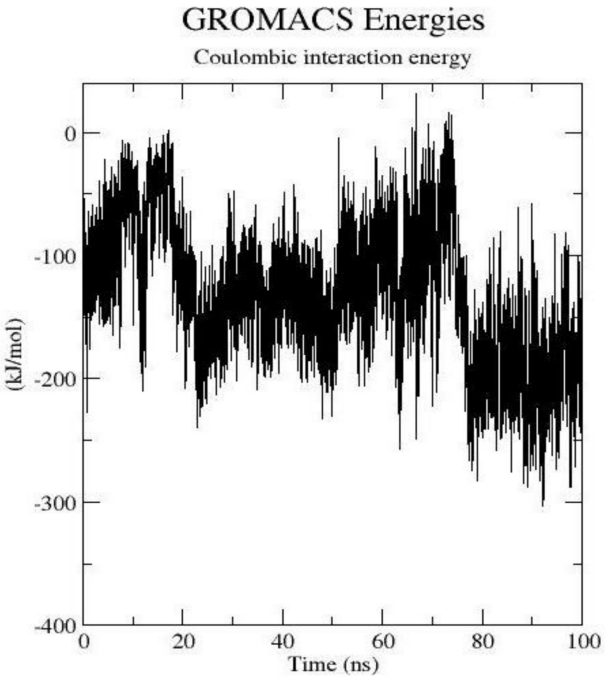

Figure 15. Coulombic electrostatic interaction energy between hyperoside and SARS-CoV-2 RdRp during MD simulation, showing an average value of −131.994 kJ/mol.

Furthermore, Lennard-Jones energy was proposed by Sir John Edward Lennard-Jones and describes the potential interaction energy between two non-bonding molecules. Lennard-Jones energy computes the difference between several attractive forces, such as dipole–dipole and London interactions, as well as repulsive forces [64]. The average Lennard-Jones energy between hyperoside and SARS-CoV-2 RdRp was computed to be −67.0503 kJ/mol (Figure 16), indicating that hyperoside has a high affinity towards the RNA-dependent RNA polymerase.

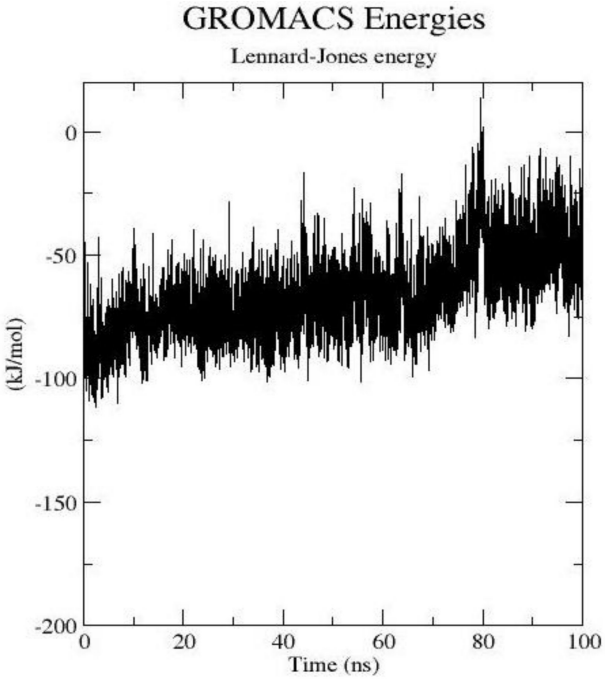

Figure 16. Lennard-Jones interaction energy between hyperoside and SARS-CoV-2 RdRp during the MD simulation, showing an average value of −67.0503 kJ/mol.

For a closer look at the electrostatic interactions between hyperoside and SARS-CoV-2 RNA-dependent RNA polymerase, the VMD program was used to calculate the number of H-bonds formed over the course of the simulation. The analysis showed that during most of the simulation time, the number of stable H-bonds varies between 2 and 3, and reaches 4 during the last 35 ns of the simulation (Figure 17), indicating the strength of the SARS-CoV-2 RdRp-ligand binding.

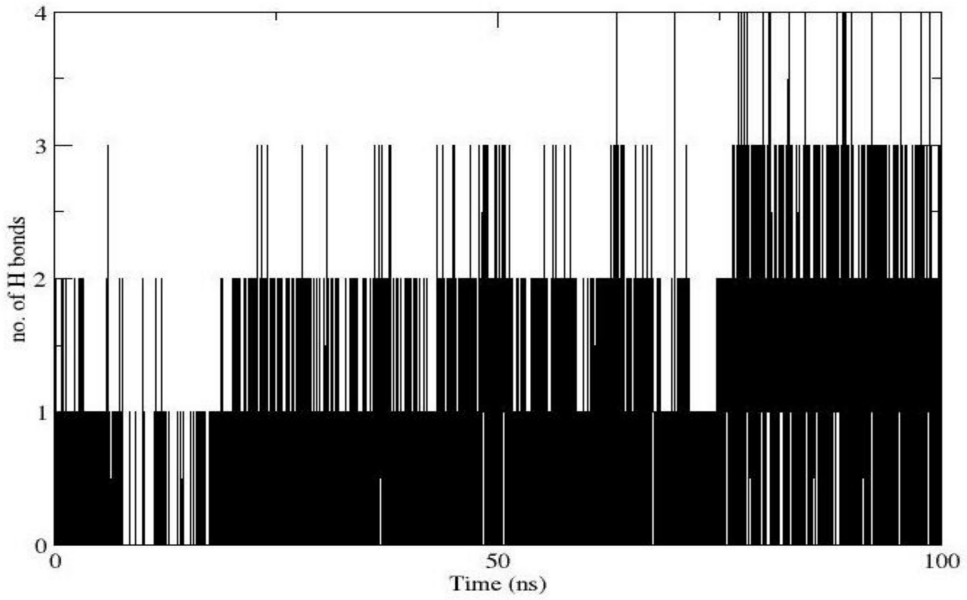

Figure 17. Changes in the number of H-bonds formed between hyperoside and SARS-CoV-2 RdRp.

3. Methods

3.1. Molecular Similarity Detection

Discovery studio 4.0 software was used (see method part in Supplementary data).

3.2. Fingerprint Studies

Discovery studio 4.0 software [65–67] was used (see method part in Supplementary data).

3.3. Docking Studies

Docking studies were performed with target enzymes using Discovery studio software [68,69] (see method part in Supplementary data).

3.4. Molecular Dynamics Simulation

The system was prepared using the web-based CHARMM-GUI [70–73] interface utilizing CHARMM36 force field and NAMD 2.13 packages [74]. The TIP3P explicit solvation model was used (See Supplementary data).

4. Conclusions

Among 3009 clinical and FDA-approved drugs, 5 (Aloin **359**, Baicalin **456**, Cefadroxil **1273**, Sophoricoside **1459**, Hyperoside **2109**, and Vitexin **2286**) were determined as the most potent inhibitors of SARS-CoV-2 RdRp(PDB ID: 7BV2). The study depended on a multi-phase in silico approach that included molecular fingerprint studies of RTP (the co-crystallized ligand of the examined protein), structure similarity experiments of RTP, molecular docking experiments of SARS-CoV-2 RdRp, and MD-simulation experiments for Hyperoside **2109** against SARS-CoV-2 RdRp for 100 ns. These results open a window of hope to find treatment through further in vitro and in vivo examinations for the determined compounds against COVID-19.

Supplementary Materials: The detailed experimental data can be downloaded at: https://www.mdpi.com/article/10.3390/pr10030530/s1.

Author Contributions: Conceptualization, A.M.M. and I.H.E.; Data curation, A.M.M. and I.H.E. Project administration, A.M.M. and I.H.E.; Supervision, A.M.M. and I.H.E.; Funding acquisition, A.B. and B.A.A.; Software, E.B.E., H.E., T.H.I., M.A. and R.K.A.; Writing—review & editing, E.B.E., A.B., B.A.A., A.M.M. and I.H.E. All authors have read and agreed to the published version of the manuscript.

Funding: This research was funded by Princess Nourah bint Abdulrahman University Researchers Supporting Project number (PNURSP2022R142), Princess Nourah bint Abdulrahman University, Riyadh, Saudi Arabia. Amany Belal would like to thank Taif University Researchers Supporting Project number (TURSP-2020/35), Taif University, Taif, Saudi Arabia.

Institutional Review Board Statement: Not applicable.

Informed Consent Statement: Not applicable.

Data Availability Statement: All data is contained in the published article.

Acknowledgments: Amany Belal would like to thank Taif University Researchers Supporting Project number (TURSP-2020/35), Taif University, Taif, Saudi Arabia.

Conflicts of Interest: The authors declare no conflict of interest.

References

1. WHO. *WHO Coronavirus (COVID-19) Dashboard*; WHO: Geneva, Switzerland, 2022.
2. Ciociola, A.A.; Cohen, L.B.; Kulkarni, P.; Kefalas, C.; Buchman, A.; Burke, C.; Cain, T.; Connor, J.; Ehrenpreis, E.D.; Fang, J.; et al. How drugs are developed and approved by the FDA: Current process and future directions. *Am. J. Gastroenterol.* **2014**, *109*, 620–623. [CrossRef] [PubMed]
3. Brown, D.G.; Wobst, H.J. A decade of FDA-approved drugs (2010–2019): Trends and future directions. *J. Med. Chem.* **2021**, *64*, 2312–2338. [CrossRef]
4. Pushpakom, S.; Iorio, F.; Eyers, P.A.; Escott, K.J.; Hopper, S.; Wells, A.; Doig, A.; Guilliams, T.; Latimer, J.; McNamee, C.; et al. Drug repurposing: Progress, challenges and recommendations. *Nat. Rev. Drug Discov.* **2019**, *18*, 41–58. [CrossRef] [PubMed]
5. Chan, H.C.S.; Shan, H.; Dahoun, T.; Vogel, H.; Yuan, S. Advancing drug discovery via artificial intelligence. *Trends Pharmacol. Sci.* **2019**, *40*, 592–604. [CrossRef] [PubMed]
6. Xu, J.; Hagler, A. Chemoinformatics and drug discovery. *Molecules* **2002**, *7*, 566–600. [CrossRef]
7. Engel, T. Basic overview of chemoinformatics. *J. Chem. Inf. Model.* **2006**, *46*, 2267–2277. [CrossRef] [PubMed]
8. Shaker, B.; Ahmad, S.; Lee, J.; Jung, C.; Na, D. In silico methods and tools for drug discovery. *Comput. Biol. Med.* **2021**, *137*, 104851. [CrossRef] [PubMed]
9. Zhang, W.; Pei, J.; Lai, L. Computational multitarget drug design. *J. Chem. Inf. Model.* **2017**, *57*, 403–412. [CrossRef]
10. Youssef, M.I.; Zhou, Y.; Eissa, I.H.; Wang, Y.; Zhang, J.; Jiang, L.; Hu, W.; Qi, J.; Chen, Z. Tetradecyl 2,3-dihydroxybenzoate alleviates oligodendrocyte damage following chronic cerebral hypoperfusion through IGF-1 receptor. *Neurochem. Int.* **2020**, *138*, 104749. [CrossRef]
11. Zhong, F.; Xing, J.; Li, X.; Liu, X.; Fu, Z.; Xiong, Z.; Lu, D.; Wu, X.; Zhao, J.; Tan, X.; et al. Artificial intelligence in drug design. *Sci. China Life Sci.* **2018**, *61*, 1191–1204. [CrossRef]
12. Hagras, M.; El Deeb, M.A.; Elzahabi, H.S.A.; Elkaeed, E.B.; Mehany, A.B.M.; Eissa, I.H. Discovery of new quinolines as potent colchicine binding site inhibitors: Design, synthesis, docking studies, and anti-proliferative evaluation. *J. Enzym. Inhib. Med. Chem.* **2021**, *36*, 640–658. [CrossRef]
13. Eissa, I.H.; Dahab, M.A.; Ibrahim, M.K.; Alsaif, N.A.; Alanazi, A.; Eissa, S.I.; Mehany, A.B.; Beauchemin, A.M. Design and discovery of new antiproliferative 1,2,4-triazin-3(2H)-ones as tubulin polymerization inhibitors targeting colchicine binding site. *Bioorg. Chem.* **2021**, *112*, 104965. [CrossRef]
14. Eissa, I.H.; El-Helby, A.-G.A.; Mahdy, H.A.; Khalifa, M.M.; Elnagar, H.A.; Mehany, A.B.; Metwaly, A.M.; Elhendawy, M.A.; Radwan, M.M.; El Sohly, M.A.; et al. Discovery of new quinazolin-4(3H)-ones as VEGFR-2 inhibitors: Design, synthesis, and anti-proliferative evaluation. *Bioorg. Chem.* **2020**, *105*, 104380. [CrossRef]
15. El-Adl, K.; El-Helby, A.-G.A.; Ayyad, R.R.; Mahdy, H.A.; Khalifa, M.M.; Elnagar, H.A.; Mehany, A.B.; Metwaly, A.M.; Elhendawy, M.A.; Radwan, M.M.; et al. Design, synthesis, and anti-proliferative evaluation of new quinazolin-4(3H)-ones as potential VEGFR-2 inhibitors. *Bioorg. Med. Chem.* **2021**, *29*, 115872. [CrossRef]
16. El-Helby, A.-G.A.; Ayyad, R.R.A.; El-Adl, K.; Sakr, H.; Abd-Elrahman, A.A.; Eissa, I.H.; Elwan, A. Design, molecular docking and synthesis of some novel 4-acetyl-1-substituted-3,4-dihydroquinoxalin-2(1H)-one derivatives for anticonvulsant evaluation as AMPA-receptor antagonists. *Med. Chem. Res.* **2016**, *25*, 3030–3046. [CrossRef]

17. Kairys, V.; Baranauskiene, L.; Kazlauskiene, M.; Matulis, D.; Kazlauskas, E. Binding affinity in drug design: Experimental and computational techniques. *Expert Opin. Drug Discov.* **2019**, *14*, 755–768. [CrossRef]
18. Al-Warhi, T.; El Kerdawy, A.M.; Aljaeed, N.; Ismael, O.E.; Ayyad, R.R.; Eldehna, W.M.; Abdel-Aziz, H.A.; Al-Ansary, G.H. Synthesis, biological evaluation and in silico studies of certain oxindole–indole conjugates as anticancer CDK inhibitors. *Molecules* **2020**, *25*, 2031. [CrossRef]
19. Suleimen, Y.M.; Metwaly, A.M.; Mostafa, A.E.; Elkaeed, E.B.; Liu, H.-W.; Basnet, B.B.; Suleimen, R.N.; Ishmuratova, M.Y.; Turdybekov, K.M.; Van Hecke, K. Isolation, crystal structure, and in silico aromatase inhibition activity of ergosta-5, 22-dien-3β-ol from the *Fungus Gyromitra esculenta*. *J. Chem.* **2021**, *2021*, 5529786. [CrossRef]
20. March-Vila, E.; Pinzi, L.; Sturm, N.; Tinivella, A.; Engkvist, O.; Chen, H.; Rastelli, G. On the integration of in silico drug design methods for drug repurposing. *Front. Pharmacol.* **2017**, *8*, 298. [CrossRef]
21. Suleimen, Y.M.; Jose, R.A.; Suleimen, R.N.; Arenz, C.; Ishmuratova, M.Y.; Toppet, S.; Dehaen, W.; Alsfouk, B.A.; Elkaeed, E.B.; Eissa, I.H.; et al. Jusanin, a New Flavonoid from *Artemisia commutata* with an In Silico Inhibitory Potential against the SARS-CoV-2 Main Protease. *Molecules* **2022**, *27*, 1636. [CrossRef]
22. Mikherdov, A.S.; Katkova, S.A.; Novikov, A.S.; Efremova, M.M.; Reutskaya, E.Y.; Kinzhalov, M.A.J.C. (Isocyano group)· · · lone pair interactions involving coordinated isocyanides: Experimental, theoretical and CSD studies. *CrystEngComm* **2020**, *22*, 1154–1159. [CrossRef]
23. Baykov, S.V.; Mikherdov, A.S.; Novikov, A.S.; Geyl, K.K.; Tarasenko, M.V.; Gureev, M.A.; Boyarskiy, V.P. π–π noncovalent interaction involving 1,2,4- and 1,3,4-oxadiazole systems: The combined experimental, theoretical, and database study. *Molecules* **2021**, *26*, 5672. [CrossRef]
24. El-Metwally, S.A.; Abou-El-Regal, M.M.; Eissa, I.H.; Mehany, A.B.; Mahdy, H.A.; Elkady, H.; Elwan, A.; Elkaeed, E.B. Discovery of thieno[2,3-d]pyrimidine-based derivatives as potent VEGFR-2 kinase inhibitors and anti-cancer agents. *Bioorg. Chem.* **2021**, *112*, 104947. [CrossRef]
25. Alanazi, M.M.; Eissa, I.H.; Alsaif, N.A.; Obaidullah, A.J.; Alanazi, W.A.; Alasmari, A.F.; Albassam, H.; Elkady, H.; Elwan, A. Design, synthesis, docking, ADMET studies, and anticancer evaluation of new 3-methylquinoxaline derivatives as VEGFR-2 inhibitors and apoptosis inducers. *J. Enzym. Inhib. Med. Chem.* **2021**, *36*, 1760–1782. [CrossRef]
26. Alanazi, M.M.; Elwan, A.; Alsaif, N.A.; Obaidullah, A.J.; Alkahtani, H.M.; Al-Mehizia, A.A.; Alsubaie, S.M.; Taghour, M.S.; Eissa, I.H. Discovery of new 3-methylquinoxalines as potential anti-cancer agents and apoptosis inducers targeting VEGFR-2: Design, synthesis, and in silico studies. *J. Enzym. Inhib. Med. Chem.* **2021**, *36*, 1732–1750. [CrossRef]
27. Alsaif, N.A.; Taghour, M.S.; Alanazi, M.M.; Obaidullah, A.J.; Al-Mehizia, A.A.; Alanazi, M.M.; Aldawas, S.; Elwan, A.; Elkady, H. Discovery of new VEGFR-2 inhibitors based on bis([1, 2, 4]triazolo)[4,3-*a*:3′,4′-*c*]quinoxaline derivatives as anticancer agents and apoptosis inducers. *J. Enzym. Inhib. Med. Chem.* **2021**, *36*, 1093–1114. [CrossRef]
28. Alsaif, N.A.; Dahab, M.A.; Alanazi, M.M.; Obaidullah, A.J.; Al-Mehizia, A.A.; Alanazi, M.M.; Aldawas, S.; Mahdy, H.A.; Elkady, H. New quinoxaline derivatives as VEGFR-2 inhibitors with anticancer and apoptotic activity: Design, molecular modeling, and synthesis. *Bioorg. Chem.* **2021**, *110*, 104807. [CrossRef]
29. El-Adl, K.; Ibrahim, M.-K.; Alesawy, M.S.; Eissa, I.H. [1,2,4]triazolo[4,3-c]quinazoline and bis([1,2,4]triazolo)[4,3-a:4′,3′-c]quinazoline derived DNA intercalators: Design, synthesis, in silico ADMET profile, molecular docking and anti-proliferative evaluation studies. *Bioorg. Med. Chem.* **2021**, *30*, 115958. [CrossRef]
30. Nesterov, P.; Shilovskikh, V.; Sokolov, A.; Gurzhiy, V.; Novikov, A.; Timralieva, A.; Belogub, E.; Kondratyuk, N.; Orekhov, N.; Skorb, E. Encapsulation of rhodamine 6G dye molecules for affecting symmetry of supramolecular crystals of melamine-barbiturate. *Symmetry* **2021**, *13*, 1119. [CrossRef]
31. Imoro, N.; Shilovskikh, V.V.; Nesterov, P.V.; Timralieva, A.A.; Gets, D.; Nebalueva, A.; Lavrentev, F.V.; Novikov, A.S.; Kondratyuk, N.D.; Orekhov, N.D.; et al. Biocompatible pH-degradable functional capsules based on melamine cyanurate self-assembly. *ACS Omega* **2021**, *6*, 17267–17275. [CrossRef] [PubMed]
32. Alesawy, M.; Abdallah, A.; Taghour, M.; Elkaeed, E.; Eissa, I.H.; Metwaly, A. In silico studies of some isoflavonoids as potential candidates against COVID-19 targeting human ACE2 (hACE2) and viral main protease (M^{pro}). *Molecules* **2021**, *26*, 2806. [CrossRef] [PubMed]
33. El-Demerdash, A.; Metwaly, A.M.; Hassan, A.; El-Aziz, A.; Mohamed, T.; Elkaeed, E.B.; Eissa, I.H.; Arafa, R.K.; Stockand, J.D. Comprehensive virtual screening of the antiviral potentialities of marine polycyclic guanidine alkaloids against SARS-CoV-2 (COVID-19). *Biomolecules* **2021**, *11*, 460. [CrossRef]
34. Jalmakhanbetova, R.I.; Suleimen, Y.M.; Oyama, M.; Elkaeed, E.B.; Eissa, I.H.; Suleimen, R.N.; Metwaly, A.M.; Ishmuratova, M.Y. Isolation and in silico anti-COVID-19 main protease (Mpro) activities of flavonoids and a sesquiterpene lactone from *Artemisia sublessingiana*. *J. Chem.* **2021**, *2021*, 5547013. [CrossRef]
35. Eissa, I.H.; Khalifa, M.M.; Elkaeed, E.B.; Hafez, E.E.; Alsfouk, A.A.; Metwaly, A.M. In silico exploration of potential natural inhibitors against SARS-CoV-2 nsp10. *Molecules* **2021**, *26*, 6151. [CrossRef]
36. Alesawy, M.S.; Elkaeed, E.B.; Alsfouk, A.A.; Metwaly, A.M.; Eissa, I. In silico screening of semi-synthesized compounds as potential inhibitors for SARS-CoV-2 papain-like protease: Pharmacophoric features, molecular docking, ADMET, toxicity and DFT studies. *Molecules* **2021**, *26*, 6593. [CrossRef]
37. Schneider, G.; Tanrikulu, Y.; Schneider, P. Self-organizing molecular fingerprints: A ligand-based view on drug-like chemical space and off-target prediction. *Future Med. Chem.* **2009**, *1*, 213–218. [CrossRef]

38. Vidal, D.; Garcia-Serna, R.; Mestres, J. Ligand-based approaches to in silico pharmacology. In *Methods in Pharmacology and Toxicology*; Springer Science and Business Media LLC: Berlin, Germany, 2010; Volume 672, pp. 489–502.
39. Briem, H.; Kuntz, I.D. Molecular similarity based on DOCK-generated fingerprints. *J. Med. Chem.* **1996**, *39*, 3401–3408. [CrossRef]
40. Willett, P. Similarity searching using 2D structural fingerprints. *Methods Pharmacol. Toxicol.* **2010**, *672*, 133–158.
41. Spackman, M.A.; McKinnon, J.J. Fingerprinting intermolecular interactions in molecular crystals. *CrystEngComm* **2002**, *4*, 378–392. [CrossRef]
42. Chu, H.; He, Q.-X.; Wang, J.; Hu, Y.; Wang, Y.-Q.; Lin, Z.-H. In silico design of novel benzohydroxamate-based compounds as inhibitors of histone deacetylase 6 based on 3D-QSAR, molecular docking, and molecular dynamics simulations. *New J. Chem.* **2020**, *44*, 21201–21210. [CrossRef]
43. Ieritano, C.; Campbell, J.L.; Hopkins, W.S. Predicting differential ion mobility behaviour in silico using machine learning. *Analyst* **2021**, *146*, 4737–4743. [CrossRef]
44. Taha, M.; Ismail, N.H.; Ali, M.; Rashid, U.; Imran, S.; Uddin, N.; Khan, K.M. Molecular hybridization conceded exceptionally potent quinolinyl-oxadiazole hybrids through phenyl linked thiosemicarbazide antileishmanial scaffolds: In silico validation and SAR studies. *Bioorg. Chem.* **2017**, *71*, 192–200. [CrossRef]
45. Heikamp, K.; Bajorath, J. How do 2D fingerprints detect structurally diverse active compounds? Revealing compound subset-specific fingerprint features through systematic selection. *J. Chem. Inf. Model.* **2011**, *51*, 2254–2265. [CrossRef]
46. Opo, F.A.D.M.; Rahman, M.M.; Ahammad, F.; Ahmed, I.; Bhuiyan, M.A.; Asiri, A.M. Structure based pharmacophore modeling, virtual screening, molecular docking and ADMET approaches for identification of natural anti-cancer agents targeting XIAP protein. *Sci. Rep.* **2021**, *11*, 4049. [CrossRef]
47. Duan, J.; Dixon, S.L.; Lowrie, J.F.; Sherman, W. Analysis and comparison of 2D fingerprints: Insights into database screening performance using eight fingerprint methods. *J. Mol. Graph. Model.* **2010**, *29*, 157–170. [CrossRef]
48. Sastry, M.; Lowrie, J.F.; Dixon, S.L.; Sherman, W. Large-scale systematic analysis of 2D fingerprint methods and parameters to improve virtual screening enrichments. *J. Chem. Inf. Model.* **2010**, *50*, 771–784. [CrossRef]
49. Kogej, T.; Engkvist, O.; Blomberg, A.N.; Muresan, S. Multifingerprint based similarity searches for targeted class compound selection. *J. Chem. Inf. Model.* **2006**, *46*, 1201–1213. [CrossRef]
50. Maggiora, G.; Vogt, M.; Stumpfe, D.; Bajorath, J. Molecular similarity in medicinal chemistry: Miniperspective. *J. Med. Chem.* **2014**, *57*, 3186–3204. [CrossRef] [PubMed]
51. Muegge, I.; Mukherjee, P. An overview of molecular fingerprint similarity search in virtual screening. *Expert Opin. Drug Discov.* **2015**, *11*, 137–148. [CrossRef] [PubMed]
52. Turchi, M.; Cai, Q.; Lian, G. An evaluation of in-silico methods for predicting solute partition in multiphase complex fluids—A case study of octanol/water partition coefficient. *Chem. Eng. Sci.* **2019**, *197*, 150–158. [CrossRef]
53. Sullivan, K.M.; Enoch, S.J.; Ezendam, J.; Sewald, K.; Roggen, E.L. Cochrane, an adverse outcome pathway for sensitization of the respiratory tract by low-molecular-weight chemicals: Building evidence to support the utility of in vitro and in silico methods in a regulatory context. *Appl. In Vitro Toxicol.* **2017**, *3*, 213–226. [CrossRef]
54. Altamash, T.; Amhamed, A.; Aparicio, S.; Atilhan, M. Effect of hydrogen bond donors and acceptors on CO_2 absorption by deep eutectic solvents. *Processes* **2020**, *8*, 1533. [CrossRef]
55. Wan, Y.; Tian, Y.; Wang, W.; Gu, S.; Ju, X.; Liu, G. In silico studies of diarylpyridine derivatives as novel HIV-1 NNRTIs using docking-based 3D-QSAR, molecular dynamics, and pharmacophore modeling approaches. *RSC Adv.* **2018**, *8*, 40529–40543. [CrossRef]
56. Escamilla-Gutiérrez, A.; Ribas-Aparicio, R.M.; Córdova-Espinoza, M.G.; Castelán-Vega, J.A. In silico strategies for modeling RNA aptamers and predicting binding sites of their molecular targets. *Nucleosides Nucleotides Nucleic Acids* **2021**, *40*, 798–807. [CrossRef]
57. Kaushik, A.C.; Kumar, A.; Bharadwaj, S.; Chaudhary, R.; Sahi, S. *Ligand-Based Approach for In-Silico Drug Designing*; Springer Science and Business Media: Berlin, Germany, 2018; pp. 11–19.
58. Jain, A.N. Morphological similarity: A 3D molecular similarity method correlated with protein-ligand recognition. *J. Comput. Mol. Des.* **2000**, *14*, 199–213. [CrossRef]
59. Zhang, H.; Ren, J.-X.; Ma, J.-X.; Ding, L. Development of an in silico prediction model for chemical-induced urinary tract toxicity by using naïve Bayes classifier. *Mol. Divers.* **2019**, *23*, 381–392. [CrossRef]
60. Zhao, J.; Tian, S.; Lu, D.; Yang, J.; Zeng, H.; Zhang, F.; Tu, D.; Ge, G.; Zheng, Y.; Shi, T.; et al. Systems pharmacological study illustrates the immune regulation, anti-infection, anti-inflammation, and multi-organ protection mechanism of Qing-Fei-Pai-Du decoction in the treatment of COVID-19. *Phytomedicine* **2021**, *85*, 153315. [CrossRef] [PubMed]
61. Wu, L.-L.; Yang, X.-B.; Huang, Z.-M.; Liu, H.-Z.; Wu, G.-X. In vivo and in vitro antiviral activity of hyperoside extracted from *Abelmoschus manihot* (L) medik. *Acta Pharmacol. Sin.* **2007**, *28*, 404–409. [CrossRef] [PubMed]
62. Kim, S.-J.; Um, J.-Y.; Hong, S.-H.; Lee, J.-Y. Anti-inflammatory activity of hyperoside through the suppression of nuclear factor-κB activation in mouse peritoneal macrophages. *Am. J. Chin. Med.* **2011**, *39*, 171–181. [CrossRef] [PubMed]
63. Landau, L.D. *The Kinetic Equation in the Case of Coulomb Interaction*; General Dynamics/Astronautics: San Diego, CA, USA, 1958.
64. Tahery, R.; Modares, H. Lennard-jones energy parameter for pure fluids from scaled particle theory. *Iran. J. Chem. Chem. Eng.* **2007**, *26*, 1–8.

65. Yousef, R.G.; Sakr, H.M.; Eissa, I.H.; Mehany, A.B.M.; Metwaly, A.M.; Elhendawy, M.A.; Radwan, M.M.; El Sohly, M.A.; Abulkhair, H.S.; El-Adl, K. New quinoxaline-2(1H)-ones as potential VEGFR-2 inhibitors: Design, synthesis, molecular docking, ADMET profile and anti-proliferative evaluations. *New J. Chem.* **2021**, *45*, 16949–16964. [CrossRef]
66. Amer, H.H.; Alotaibi, S.H.; Trawneh, A.H.; Metwaly, A.M.; Eissa, I.H. Anticancer activity, spectroscopic and molecular docking of some new synthesized sugar hydrazones, Arylidene and α-Aminophosphonate derivatives. *Arab. J. Chem.* **2021**, *14*, 103348. [CrossRef]
67. Alesawy, M.S.; Al-Karmalawy, A.A.; Elkaeed, E.B.; Alswah, M.; Belal, A.; Taghour, M.S.; Eissa, I.H. Design and discovery of new 1,2,4-triazolo[4,3- c]quinazolines as potential DNA intercalators and topoisomerase II inhibitors. *Arch. Pharm.* **2021**, *354*, e2000237. [CrossRef]
68. Parmar, D.R.; Soni, J.Y.; Guduru, R.; Rayani, R.H.; Kusurkar, R.V.; Vala, A.G.; Talukdar, S.N.; Eissa, I.H.; Metwaly, A.M.; Khalil, A.; et al. Discovery of new anticancer thiourea-azetidine hybrids: Design, synthesis, in vitro antiproliferative, SAR, in silico molecular docking against VEGFR-2, ADMET, toxicity, and DFT studies. *Bioorg. Chem.* **2021**, *115*, 105206. [CrossRef]
69. Protein Data Bank, 2020. 2021. Available online: https://www.rcsb.org/structure/4OW0 (accessed on 2 October 2021).
70. Jo, S.; Kim, T.; Iyer, V.G.; Im, W. CHARMM-GUI: A web-based graphical user interface for CHARMM. *J. Comput. Chem.* **2008**, *29*, 1859–1865. [CrossRef]
71. Brooks, B.R.; Brooks, C.L., III; MacKerell, A.D., Jr.; Nilsson, L.; Petrella, R.J.; Roux, B.; Won, Y.; Archontis, G.; Bartels, C.; Boresch, S.; et al. CHARMM: The biomolecular simulation program. *J. Comput. Chem.* **2009**, *30*, 1545–1614. [CrossRef]
72. Lee, J.; Cheng, X.; Swails, J.M.; Yeom, M.S.; Eastman, P.K.; Lemkul, J.; Wei, S.; Buckner, J.; Jeong, J.C.; Qi, Y.; et al. CHARMM-GUI input generator for NAMD, GROMACS, AMBER, OpenMM, and CHARMM/OpenMM simulations using the CHARMM36 additive force field. *J. Chem. Theory Comput.* **2016**, *12*, 405–413. [CrossRef]
73. Best, R.B.; Zhu, X.; Shim, J.; Lopes, P.E.; Mittal, J.; Feig, M.; Mackerell, D.A., Jr. Optimization of the additive CHARMM all-atom protein force field targeting improved sampling of the backbone phi, psi and side-chain chi(1) and chi(2) dihedral angles. *J. Chem. Theory Comput.* **2012**, *8*, 3257–3273. [CrossRef]
74. Phillips, J.C.; Braun, R.; Wang, W.; Gumbart, J.; Tajkhorshid, E.; Villa, E.; Chipot, C.; Skeel, R.D.; Kalé, L.; Schulten, K. Scalable molecular dynamics with NAMD. *J. Comput. Chem.* **2005**, *26*, 1781–1802. [CrossRef]